ISSN (Print) 1226-1750
ISSN (Online) 2233-6656
Journal of Magnetics 30(4), 533-543 (2025) https://doi.org/10.4283/JMAG.2025.30.4.533

Theoretical Analysis and Experimental Study on the Magnets' Structure of Magnetic Stirrer

Jun Yan[1†], Zhipeng Wang[2†], Ziyang Li[2], Dehui Wu[2], Jiawei Liu[2]*, Qipeng Jin[3], and Zhanpeng Gong[3]

[1]Nuclear Technology Support Center of CAEA, Beijing 100160, China
[2]China Nuclear Power Engineering Co., Ltd., Beijing Chemical Industry Research and Design Institute, Chemical Equipment Institute, Beijing 100840, China
[3]Hangzhou Jingye Intelligent Technology Co., LTD., Hangzhou 310000, China

(Received 30 September 2025, Received in final form 10 December 2025, Accepted 10 December 2025)

To address synchronization loss, centering difficulties, low magnetic field utilization, and adaptation challenges in sealed and space-limited scenarios within nuclear/chemical industries, this study optimized active magnet and stirrer structures through theoretical, simulation, and experimental investigations. A magnetic force model was established and verified via Maxwell simulations. It was found that axial magnetization of the active magnet provides effective centering magnetic force, while a stirrer composed of permanent magnets and silicon steel exhibits superior magnetic performance. Experimental results validated the theoretical and simulation analyses, confirming that the proposed structure resolves centering and synchronization issues in conventional designs. The optimized axial-magnetized active magnet and permanent magnet-soft magnetic composite stirrer significantly enhance magnetic field utilization and operational stability, offering a reliable solution for stirring and dispersion in sealed nuclear environments.

Keywords : magnetic stirrer, permanent magnet, structural optimization, magnetic field, finite element simulation

1. Introduction

Stirring is a crucial unit operation in the nuclear industry and chemical engineering. For instance, numerous processes involving homogenization, extraction, dissolution, crystallization, emulsion preparation, and liquid-phase reactions require stirring in some form [1]. With the advancement of science and technology, magnetic stirrers are widely used due to their simple structure and high stirring efficiency. Existing magnetic stirrers are mainly classified into two types: stirrer rotor structures [2] and magnetic coupling structures [3]. The magnetic coupling structure can transmit large torques [4], making it suitable for large-scale reactors to accelerate material reactions and achieve material homogenization inside the reactor [5]. Magnetic stirrers have long maintained an advantageous position in mechanical stirring equipment due to their unique vortex-generation capability, excellent mixing efficiency, and ease of operation [6, 7]. Such systems significantly improve mixing uniformity and reduce maintenance costs by virtue of their simplified mechanical structure and adaptability to different vessel shapes. For magnetic stirrers used in the nuclear industry and chemical engineering, container sealing needs to be prioritized; thus, magnetic stirrers that do not require insertion/removal of internal rotors and have a long service life have been widely adopted [8]. To ensure sufficient reactions, an external magnet is required to rotate and drive the liquid in the reaction vessel to form a vortex. Yusuf Oner [9] focused on the optimal design and three-dimensional static magnetic analysis of permanent magnet spherical rotors. They embedded a four-pole permanent magnet structure into a Teflon matrix to form a spherical surface, addressing the issues of complex processing and high cost associated with traditional single-magnet rotor structures. Permanent magnet spherical rotors are typically applied in high-power magnetic stirrers; however, for small-scale stirrers, spherical rotors

*Corresponding author: Tel: +8618310375506
e-mail: 1196818395@qq.com
†These authors contributed equally to this work.

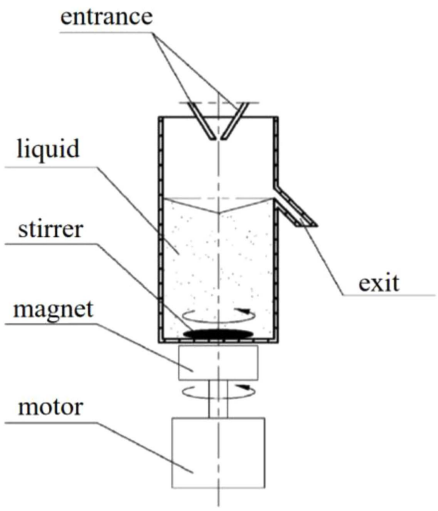

Fig. 1. Principle of precipitation reactor.

usually increase the air gap between the active and driven rotors, thereby reducing the maximum rotational torque. Osman [10] developed a new structure for magnetic stirrers, which adopts an AC four-phase half-winding active rotor structure to generate a phase difference in phase currents, thereby forming a rotating magnetic field. Considering the hot-cell application of magnetic stirrers, an overly complex structure may lead to difficulties in maintenance and increased radiation impact, which is unfavorable for applications in the nuclear industry. Additionally, to prevent critical reactions, the structure should not be designed excessively large. Therefore, considering space constraints and the need to avoid radioactive material leakage caused by stirrer insertion or removal, magnetic stirrers with traditional stir bar structures have been selected as the primary stirring method for precipitation reactors. As shown in Fig. 1, the working principle of magnetic stirring involves the formation of a coupled magnetic field between the active magnet arranged outside the reaction vessel and the stir bar inside the vessel. This coupled field pulls the stir bar to rotate, causing the solution inside the reaction vessel to form a vortex. However, the stir bar of the traditional magnetic stirrer adopts a multi-segment magnet structure, specifically a "magnet-aluminum block-magnet" design. Since the aluminum block is a non-magnetic material, it cannot contribute to adsorption or magnetic field generation in the stir bar, leading to issues such as desynchronization and centering difficulties. If the active magnet below is too large, it wastes space; if too small, the adsorption effect is poor. Therefore, it is necessary to optimize the structural design of the active magnet and the stir bar.

2. Structural Design and Simulation Analysis of Magnetic Mixer

2.1. Magnetic motor scheme analysis

Fig. 2 illustrates the internal configuration of the original agitator design, featuring a multi-stage magnet structure. The configuration consists of four magnetic units arranged in a "magnet-aluminum block-magnet" sequence with three aluminum blocks. Each compact magnetic unit is radially magnetized, a configuration that enhances both the agitator's engagement and magnetic adhesion to the underlying active magnet assembly.

This design has two critical limitations. Firstly, since aluminum is non-magnetic, the lower active magnet must be similarly designed with comparable dimensions to achieve effective magnetic adhesion. Failure to meet these requirements may result in adhesion failure and inefficient use of vertical space. Secondly, the permanent magnet's magnetic flux lines struggle to form a complete loop, which weakens the magnetic field's adsorption capacity. To resolve this, we recommend replacing the active magnet with soft magnetic material demonstrating

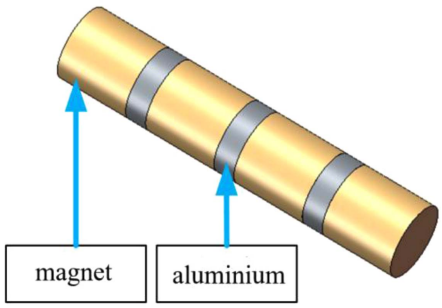

Fig. 2. (Color online) Internal structure of stirrer in traditional scheme.

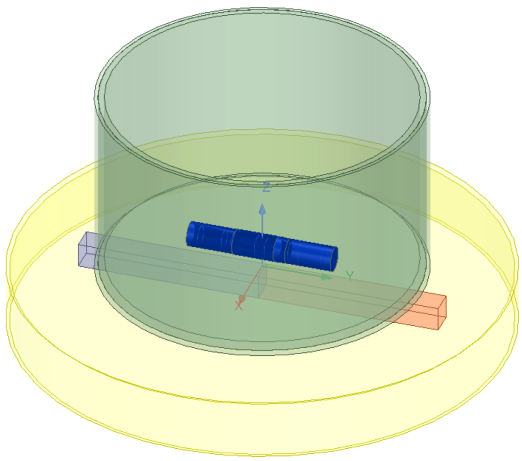

Fig. 3. (Color online) Stirrer model diagram.

superior magnetic conductivity. In this application, silicon steel (M235) has been selected as the optimal soft magnetic component.

Based on the container and magnet specifications in the design plan, the stirring system model is established as shown in Fig. 4. The stirrer is housed in a glass container nested within a stainless steel vessel, with a stainless steel box positioned below it connected to the active magnet. The container has a diameter of 200 mm, while the cylindrical stirrer measures Φ20 mm×120 mm. According to electromagnetic principles, magnetic forces originate from field gradients. The strongest gradient occurs at permanent magnet corners, requiring the long end to fully occupy the container while the narrow end should be slightly larger. Due to spatial constraints, the active magnet's height is maximized, resulting in a 250×30×30 mm permanent magnet grade N35 or higher neodymium iron boron (NdFeB) material. To prevent wear from excessive magnetic force, measurements of magnetic force under different air gaps are conducted. Alternatively, optimal air gap parameters for various solutions can be determined through trial and error, allowing precise adjustment of air gaps according to solution density.

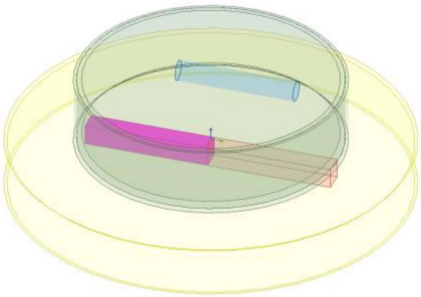

Fig. 4. (Color online) Schematic diagram of the mixer at the edge of the container.

2.2. Active Magnet Structural

For simplification of the calculation, we employ restricted element lengths in the regions with minor fluctuations in the magnetic field, with a maximum element length of 6 mm. The mesh type utilized is tetrahedral. In order to make the simulation results in the regions with fluctuations more accurate, the mesh size at the pole teeth and sealing gap is less than 0.1 mm. To account for boundary conditions and leverage our knowledge of magnet demagnetization, it is advisable to establish a vector potential boundary condition of 0 Wb/m to reduce demagnetization effects and ensure the completeness of the magnetic circuit.

Design For active magnets, the primary magnetization directions to consider are along the length (y-axis) and height (z-axis). A comparative analysis of the different magnetic forces generated by these two approaches is presented in Fig. 4. The stirring rod is positioned at the center of the container and gradually moved to its edge,

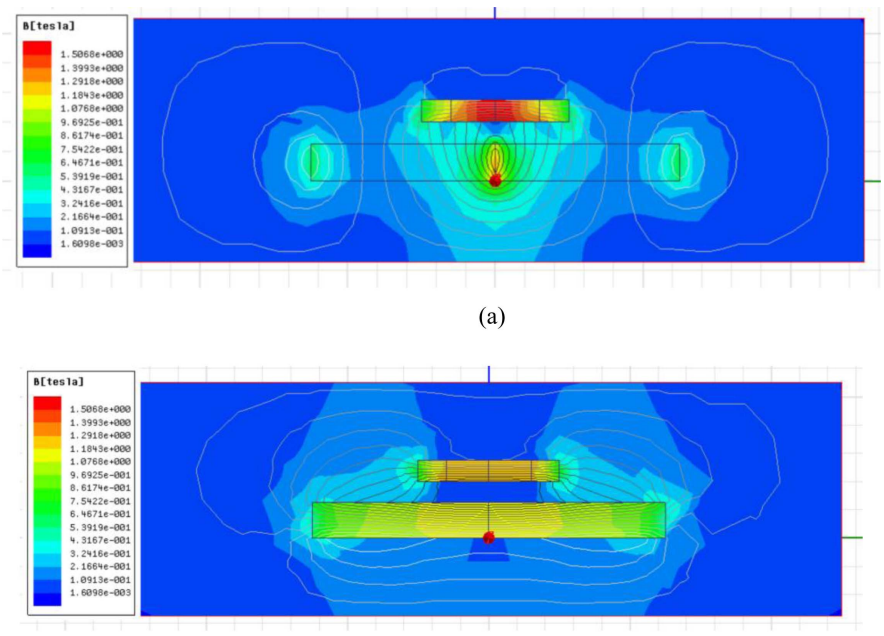

Fig. 5. (Color online) Magnetic field cloud diagram (a) Magnetic field charged along the axis (b) Magnetic field charged along the radial direction.

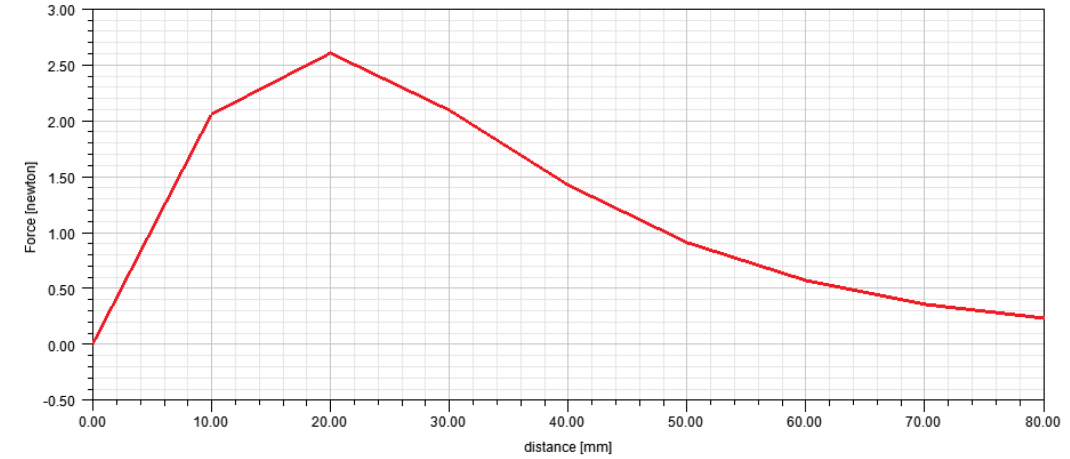

(a)

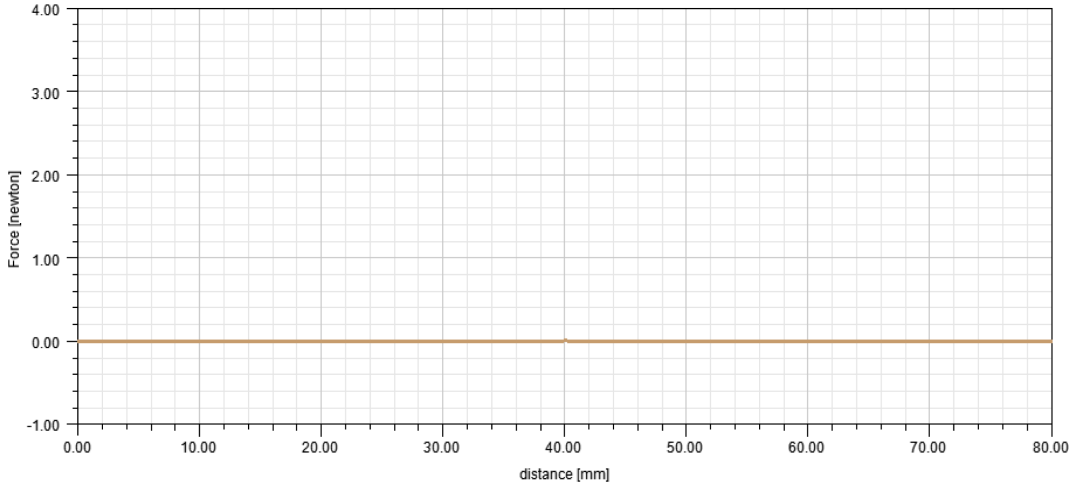

(b)

Fig. 6. (Color online) Magnetic force conditions of the stirrer at different positions (a) When the magnetic field is charged along the height direction (b) When the magnetic field is charged along the radial.

with the active magnet magnetized along both the length and height axes respectively. To ensure the stirring rod exerts no influence on the magnetic field below, it is constructed from soft magnetic material that solely serves as an adsorption mechanism. By observing the force distribution on the stirring rod, we compare the magnetic attraction magnitudes under the two magnetization methods:

Fig. 5 shows the magnetic field cloud of the active magnet when it is charged in different directions. Fig. 5(a) shows the magnetic field charged along the axis. Fig. 5(b) shows the magnetic field charged along the radial direction.

The magnetic field diagram illustrates the distribution of magnetic flux lines and magnetic strength within a field. As shown in the two diagrams, when permanent magnets have identical volumes, their magnetic intensities appear similar but exhibit fundamentally different flux direction patterns. When magnetized along the vertical axis, the opposing magnetic fields between the magnets create mutual attraction, which ultimately facilitates the positioning of the stirrer. Conversely, radial magnetization causes the active magnet's magnetic field to diverge axially, while this axial force does not assist in moving the stirrer from the edge to the center.

Fig. 6(a) shows magnetic force conditions of the stirrer at different positions when the magnetic field is charged along the height direction, (b) When the magnetic field is charged along the radial. As shown in Fig. 6, the x-axis force acts as the primary driving force during the rotor's movement from the edge to the center. The two diagrams demonstrate that when magnetized along the height

direction, the rotor experiences magnetic forces that enable its movement. However, when magnetized along the length direction, the x-axis force becomes negligible, making it nearly impossible for the rotor to achieve centripetal motion. This fundamental limitation explains why the rotor struggles to maintain proper alignment with the active magnet. To resolve this alignment challenge, the active rotor should be magnetized along the height direction.

2.3. Stirrer Structure Design

To address issues in traditional stirrer designs such as low gravitational force, step loss, and centering difficulties, two innovative magnetic core structures are proposed: The first utilizes permanent magnets with 5 φ15×20 mm cylindrical magnets (total length 100 mm along the y-axis). These N35NdFeB magnets are axially magnetized. The second structure combines permanent magnets (20 mm) with soft magnetic materials using a 20 mm permanent magnet-60 mm silicon steel-20 mm permanent magnet configuration. The permanent magnets measure φ15×20 mm cylindrical magnets magnetized axially, while the silicon steel measures φ15×60 mm. When assembled, the hybrid magnet achieves a total length of 100 mm. Comparative analysis will examine how force distribution changes with movement distance under these different magnetization methods. As shown in Fig. 7, the second design demonstrates greater force capacity, facilitating optimal repositioning. Fig. 7(a) and (b) respectly shows the variation of magnetic force on different types of stirrers with moving distance.

2.4. Misalignment Analysis

When the stirrer is adsorbed by the active magnet and positioned at the center of the container, consider a scenario where high-speed operation of the active magnet causes insufficient resistance from the solution to keep the stirrer moving in sync. This creates a non-zero

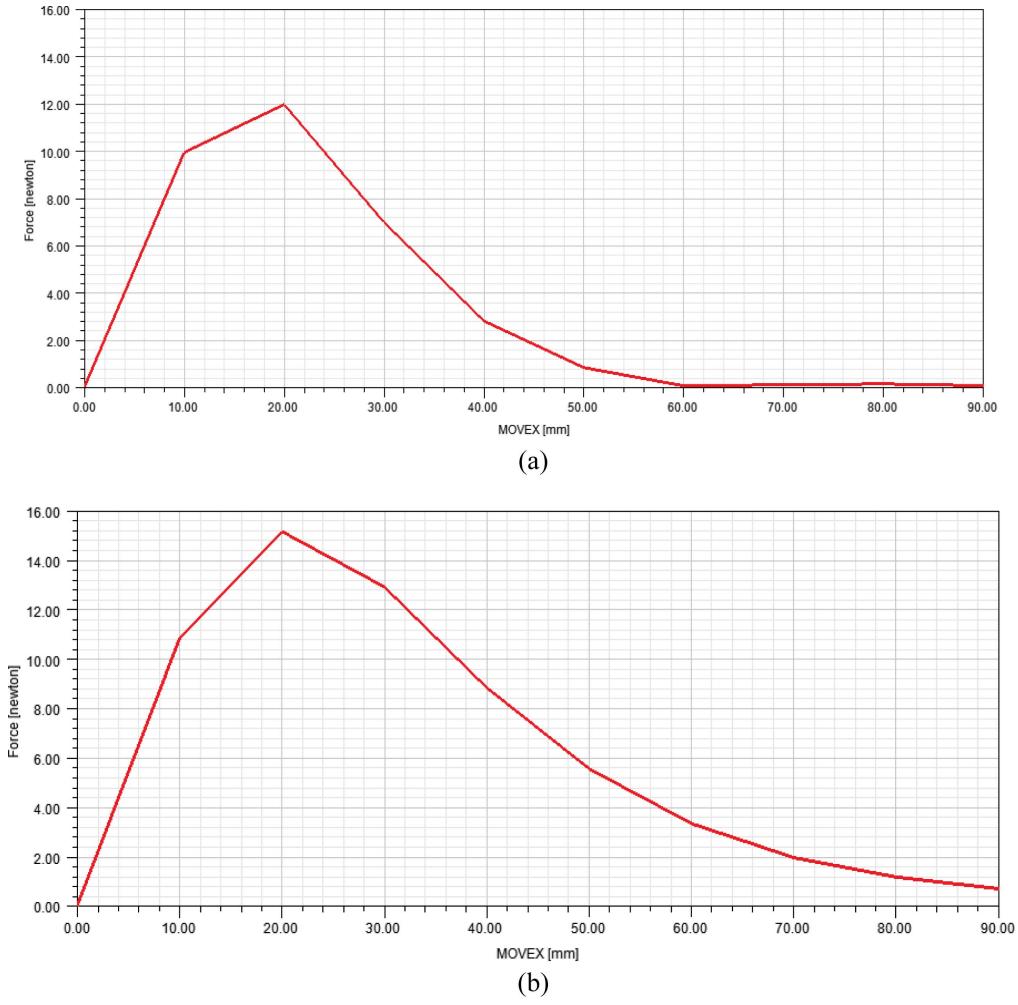

Fig. 7. (Color online) Variation of force on different types of stirrers with moving distance (a) Scheme 1 and (b) Scheme 2.

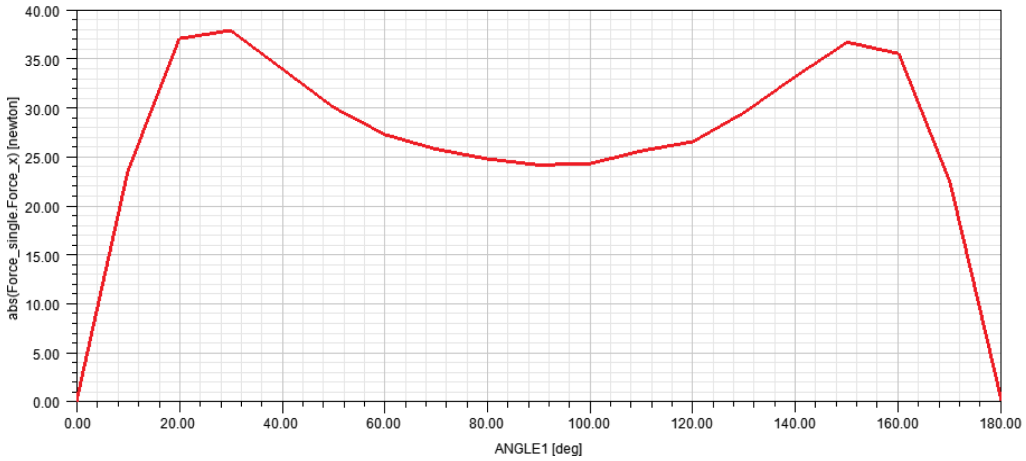

Fig. 8. (Color online) Angle θ between the stirrer and the active magnet and the relationship between their magnetic force.

horizontal angle between the two components. The investigation focuses on whether sufficient torque can be generated at this angle to maintain rotational speed synchronization. By setting the angle between the stirrer and active magnet as θ and observing its variation from 0 to 180 degrees, the analysis results are presented in Fig. 8:

As can be seen from the Fig., when the angle between them is more than 20 degrees, the traction force of the active magnet on the stirrer is stable at 25N upward, which can achieve most traction and stirring.

3. Theoretical Analysis of Magnetic Stirrers

3.1. Magnetic Circuit Analysis

To validate the magnetic force calculations from finite element simulation software, this study employs analytical methods for magnetic circuit and force analysis, as shown in Fig. 9. The magnetic system consists of two axially magnetized permanent magnets in the driving rotor and a rotor composed of permanent magnet-silicon steel-permanent magnet structure. To simplify calculations and ensure accuracy, we assume: 1) circumferential magnetic field uniformity during rotation; 2) no edge effects or rotational losses in permanent magnets; 3) low-temperature sealing conditions for magnetic fluids. Using equivalent magnetic circuit analysis, we establish mathematical analogies: magnetic potential $F = Hl$ equals electrical potential, flux density $\Phi = BA$ matches current density, and magnetic reluctance $R = l/\mu A$ corresponds to resistance. By applying Kirchhoff's laws, we derive the fundamental equations of the magnetic circuit [11, 12].

$$F = H_m l_m + Hl \tag{1}$$

$$B_m A_m = BA \tag{2}$$

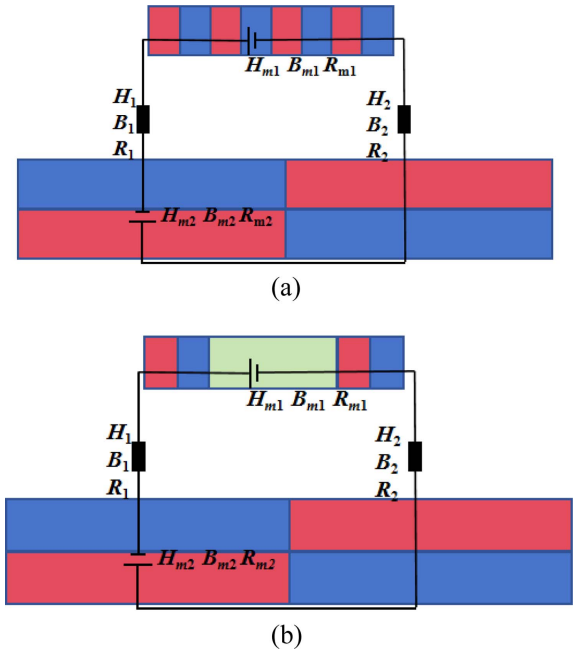

Fig. 9. (Color online) Equivalent magnetic circuit diagram of magnetic stirrer (a) first type stirrer (b) second type stirrer.

The magnetic properties of the N35 magnet used in the study were tested, with a residual magnetism of 1.18-1.23 T, coercivity of at least 836 kA/m, and maximum energy product of 263-287 kJ/m³. The permeability of magnet $\mu_A = 1.05\mu_0$. The permeability was measured under air-gap conditions with a 10 mm gap size and air permeability $\mu_A = \mu_0$. The saturation flux density of silicon steel was 1.6T, while silicon steel with magnetic fields below 1.6T exhibits significantly higher permeability than μ_0. According to the magnetoresistance formula, silicon steel's magnetic resistance can be neglected. Once the

magnetic circuit structure is determined, the working point of the permanent magnet on the hysteresis loop is also established. If there are no external magnetic sources in the magnetic circuit surrounding the permanent magnet, $F = 0$. And the total magnetic flux in the circuit equals the sum of other magnetic fluxes within the circuit $B_m A_m = B_1 A_1$. The relationship between the magnetic induction intensity from the permanent magnet and the magnetic field strength can be expressed as

$$B_m = -\frac{\mu_0 l_m A}{l \mathrm{A}_m} H_m \tag{3}$$

Then according to the maximum magnetic energy product of the actual permanent magnet, we can get

$$-\frac{\mu_0 l_m A}{l \mathrm{A}_m} H_m^2 = (BH)_{\max} \tag{4}$$

According to the aforementioned equation, it can be concluded that the working curve of permanent magnets in the stationary magnetic circuit is linear. Due to the series magnetic resistance formed by multiple permanent magnets and air gaps in the magnetic circuit, magnetic flux lines originate from the positive pole of the driving magnet, pass through the air gap into the negative pole of the agitator magnet, then exit through the silicon steel from the positive pole of the agitator magnet, cross the air gap, and enter the negative pole of the driving magnet to form a closed loop. Additionally, since the driving magnet is designed larger in volume than the agitator to maintain its centering, both structures contain leakage magnetic paths. However, these leakage paths all return directly from the positive pole of the driving magnet to its own negative pole, making them negligible. When electromagnetic coils or external magnetic fields are present, solving for magnetic field strength within the sealed gap becomes complex. In analyzing magnetic circuits with electromagnetic coils, the magnetic potential of the electromagnet and the magnetic resistance of permanent magnets must be incorporated. These magnetic fields cause permanent magnets to deviate from their working points. Given that the demagnetization curve of permanent magnets is nonlinear, analytical solutions cannot be obtained. To address this issue, we propose the following assumptions: ① Magnetic field strength within magnets and magnetic materials is uniform; ② Since magnetic flux lines follow the path of minimum resistance, we assume they enter from one side of the agitator near the driving magnet and exit from the opposite side; ③ The working point of permanent magnets lies at the maximum magnetic energy product position. Substituting these assumptions into the magnetic circuit of the magnetic stirring machine yields a new system of equations.

$$H_{m1} l_{m1} + H_{m1} l_{m2} + H_1 l_1 + H_2 l_2 = 0 \tag{5}$$

$$B_{m1} A_{m1} = B_{m2} A_{m2} = B_1 A_1 \tag{6}$$

$$\frac{B_{m1}}{B_{m2}} = \frac{H_{m2}}{H_{m1}} = \frac{A_{m2}}{A_{m1}} \tag{7}$$

The magnetic field strength H_m(A/m) generated by the permanent magnet in the formula. The magnetic induction intensity B_m(T) of the permanent magnet. The magnetic field strength H(A/m) of the air-gap reluctance near the permanent magnet. The magnetic induction intensity B(T) of the air-gap reluctance near the permanent magnet. The cross-sectional area A(m²) of the magnetic circuit. The length l(m) of the magnetic circuit.

After substituting specific data into the equations, the magnetic fields for both structural configurations can be calculated as follows: The first scheme:

$$\begin{aligned} H_{m2} &= -392\mathrm{kA/m} \\ B_{m2} &= 0.68\mathrm{T} \end{aligned} \tag{8}$$

The second scheme:

$$\begin{aligned} H_{m2} &= -440\mathrm{kA/m} \\ B_{m2} &= 0.61\mathrm{T} \end{aligned} \tag{9}$$

3.2. Calculation of Magnetic Forces on the Stirrer

3.2.1. Magnetic Forces of Permanent Magnets

At the microscopic level, permanent magnets derive their magnetism from the presence of numerous self-magnetized atoms. The electron spins and orbital motions within these atoms generate microscopic magnetic moments. These magnetic moments are orderly arranged in the material's crystal lattice, forming a stable macroscopic magnetic field. The macroscopic force experienced by a permanent magnet is the superposition of forces exerted by all microscopic magnetic dipoles. The Ampere force acting on current element $Id\boldsymbol{l}$ within the magnetic field is

$$d\boldsymbol{F} = Id\boldsymbol{l} \times \boldsymbol{B}(r) \tag{10}$$

In a uniform magnetic field, magnetic dipoles experience only rotational torque without net translational force. Net forces on magnetic dipoles only occur in non-uniform fields. When the active magnet rotates, its generated magnetic field also changes direction. This rotation creates a circumferential magnetic gradient around the

stirrer's permanent magnets. Given the small loop area of magnetic dipoles, we Taylor expand the magnetic field B(r) at the loop center and integrate the forces along the closed loop. Substituting the magnetic dipole moment $\boldsymbol{m}=I\Delta\boldsymbol{S}$ into the vector sum of current elements in the loop $\oint d\boldsymbol{l}=0$, yields the volumetric force acting on a volume element dV in a non-uniform magnetic field [13-15].

$$d\boldsymbol{F}=\boldsymbol{M}\cdot\delta\boldsymbol{B}dV \tag{11}$$

Assuming that the permanent magnet is uniformly magnetized, the calculation formula of magnetic intensity M can be obtained

$$M=B/\mu_0-H \tag{12}$$

In the formula, $\boldsymbol{m}$—magnetic dipole moment, $\boldsymbol{S}$—loop area vector, M—magnetization intensity of the permanent magnet (A/m).

The B and H of the permanent magnet are obtained in Section 3.1, and it can be calculated that the magnetic force acting on the permanent magnet element in the first stirrer structure is 101dV.

3.2.2. Magnetic Forces of Magnetic Materials

Unlike permanent magnets, magnetic materials lack inherent magnetism. Under an external magnetic field, their internal atomic magnetic moments align to generate induced magnetization. For the silicon steel used in the second type of stirrer structure, which is a linear isotropic magnetic material, the magnetization strength remains proportional to the external magnetic field when magnetized without saturation. The BH curve of silicon steel is illustrated in Fig. 10.

The magnetic induction calculated in Section 3.1 enables determination of silicon steel's magnetization

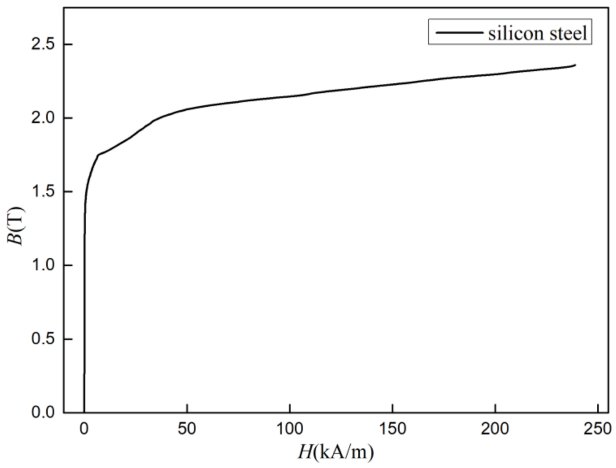

Fig. 10. The BH curve of silicon steel.

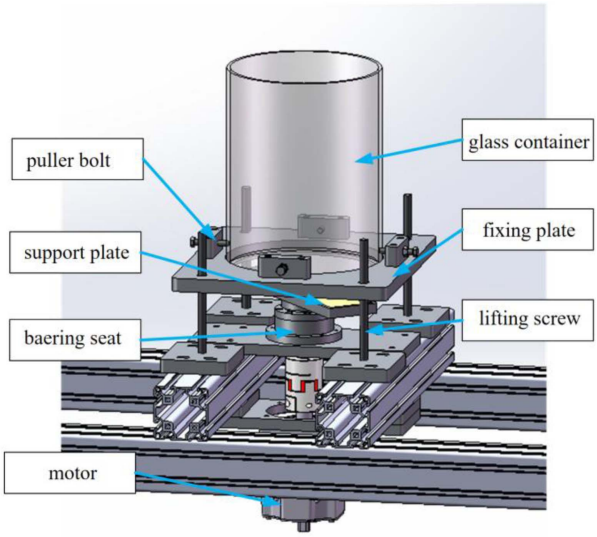

Fig. 11. (Color online) Magnetic Pole Stirring Experimental Setup.

state, with its magnetic field strength and magnetization intensity expressed as.

$$\begin{aligned} B &= 0.61\text{T} \\ H &= 77\text{A/m} \\ M &= 486\text{kA/m} \end{aligned} \tag{13}$$

Substituting these parameters into dimensional data yields the magnetic force acting on the stirrer element in the second structure: 205dV.

4. Magnetic Stirring Experiment

4.1. Magnetic Stirring Experimental Setup

The experimental setup was constructed to verify the magnetic stirring function. A servo motor connected to an active magnet drives its rotation. A container mounting plate above the active magnet is designed for holding glass containers. Four screw rods connect the mounting plate to the frame, allowing adjustment of the container's height through threaded connections to regulate the air gap between the active magnet and stirrer. The container plate features a tightening bolt for horizontal positioning and securement.

Design Simulation actual operating conditions: The container plate's base thickness is machined to 3 mm (matching the simulated chamber's thickness), with a 3 mm sleeve plate placed above it to simulate real-world glass container sleeves. The processed glass container measures 250 mm inner diameter, 450 mm height, and 5 mm wall thickness. The air gap at this time is 5 mm of

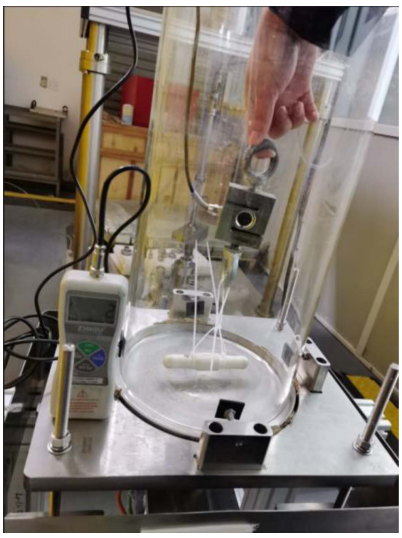

Fig. 12. (Color online) Suction force under different air gaps of the stirrer.

the thickness of the glass container.

4.2. Verification Experiment

4.2.1. Magnetic Force Measurement of Stirrers

Due to the low measurement accuracy of forces during rotation, this study modified the magnetic force measurement by pulling the stirrer away from the active magnet and recording the traction force from the tensile testing machine. Subsequently, magnetic forces between two novel stirrer structures and the active magnet under different air gaps were measured. During testing, following standard experimental procedures: adjust the container plate height to create an air gap between the plate base and the active magnet, connect the tensile device with the stirrer, place it in a glass container, grip the tension sensor to lift the stirrer until separation from the container bottom, then record the peak value of the tensile gauge, as shown in Fig. 12. The axial Magnetic Force test data for the two experimental stirrers under different air gaps are as follows:

4.2.1. Stirrer Centripetal Experiment

As shown in Fig. 13, two types of stirrer designs were

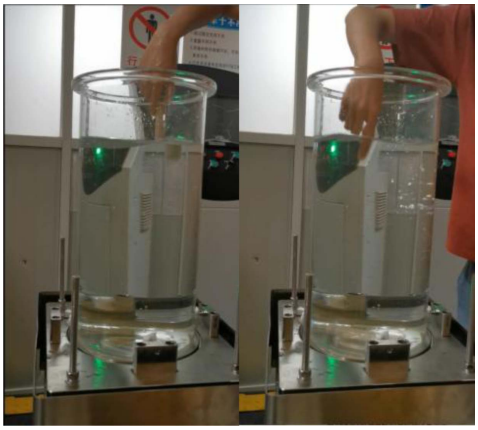

Fig. 13. (Color online) Stirrer Centripetal Experiment.

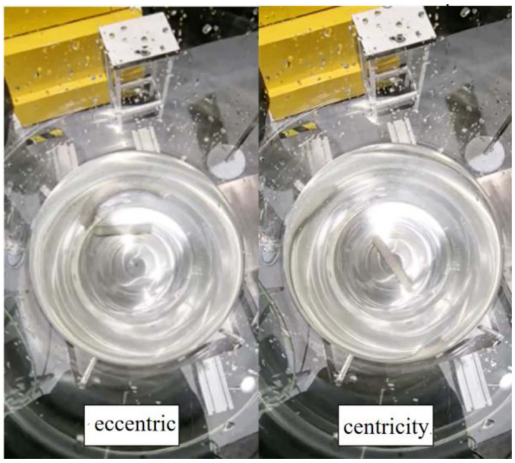

Fig. 14. (Color online) Stirrer Centrifugal Experiment.

tested by releasing them from the container's top at different angles, with 20 trials conducted. All stirrers successfully adhered to the center of the container, demonstrating centripetal functionality.

4.2.2. Stirrer Centrifugal Experiment

As shown in Fig. 14, the stirrers were stabilized off-center, while an active magnet rotated at low speed. After 10 trials, all stirrers maintained stable central adhesion, confirming centrifugal functionality.

4.2.3. Stirrer Drift Experiment

The rotation speed was adjusted from 100 to 900 rpm.

Table 1. Magnetic force under different air gaps of the two stirrers.

Type of stirrer	Magnetic forces under different air gaps/N						
	5 mm	10 mm	15 mm	20 mm	25 mm	30 mm	35 mm
permanent magnet	27	20	16	14	10	8	7
permanent magnet-silicon steel	45	38	29	24	15	10	9

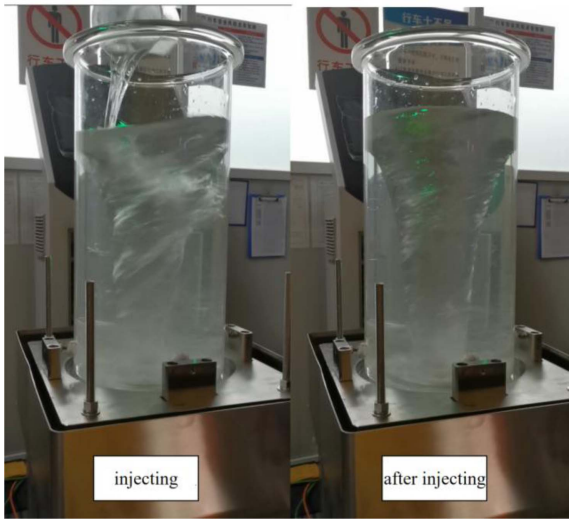

Fig. 15. (Color online) Stirrer Drift (Rotor Loss) Experiment.

Fig. 16. (Color online) Stirring Experiment.

Turbulent eddies were injected at the container's top to observe drift phenomena. As shown in Fig. 15, normal stirring remained uninterrupted throughout the experiment. Although eddy fluctuations occurred during water injection, they never disappeared and gradually returned to pre-injection states after filling. No drift or rotor loss was observed under these conditions.

4.2.4. Stirring Experiment

The second-best-performing stirrer was selected for magnetic force measurement. As shown in Fig. 16 show that: 200 rpm initially generated eddies; 500 rpm brought eddies close to the container bottom; 600 rpm established stable eddies.

4.3. Discussion

Through structural design, the key conditions for normal operation of magnetic stirring were determined. The suction force between the active magnet and stirrer must be sufficiently strong to drive the stirrer rotation while overcoming centripetal forces and various operational resistances during motion. First, simulation analysis was conducted to examine the radial force distribution on the stirrer, revealing that radial magnetization causes eccentricity and difficulties in centering. This confirmed the necessity of axial magnetization for the active magnet. The "magnet-aluminum block" assembly structure exhibits low overall magnet utilization efficiency, weak magnetic field strength, and insufficient suction force, leading to operational detraction. Additionally, the unique structure of the active magnet complicates centering due to minimal centripetal force. The study conducted theoretical and simulation comparisons between full magnet and magnet-soft magnetic material assembly structures, elucidating the macroscopic force mechanism: it is the superposition of microscopic magnetic dipole forces in non-uniform fields. By applying Kirchhoff's laws to analyze magnetic circuits, we derived magnetic field equations for the stirrer. Based on partial assumptions, magnetization conditions of permanent magnets under both structures were calculated. Subsequent derivation of magnetic force formulas confirmed that the magnet-soft magnetic material assembly structure provides stronger magnetic force. Experimental verification and simulations collectively demonstrated that this configuration delivers superior magnetic field performance. While fully permanent magnet structures provide strong magnetic fields, the magnetic gradient becomes dependent on spatial variations. Since soft magnetic materials exhibit stronger magnetization than permanent magnets, they primarily supply the magnetic force. However, this design limitation causes the stirrer to lack a defined magnetic field direction, making centering challenging. The optimal solution therefore involves a hybrid structure combining permanent magnets with soft magnetic materials. Experimental verification through magnetic force tests confirmed that this hybrid configuration outperforms all-persistent magnet designs. Centering, magnetization recovery, and phase loss tests experimentally validated the optimized design, demonstrating successful centering, magnetization recovery, and stirring functions without abnormal motion under 10 mm air-gap conditions.

5. Conclusion

This study addresses core challenges in magnetic stirrers for nuclear and chemical engineering applications, including step loss, centering difficulties, and low magnetic field utilization efficiency. Through systematic research combining theoretical modeling, simulation analysis, and experimental verification, we established a magnetic circuit and force calculation model for the magnetic coupling system. The computational mechanism of magnetic forces clarifies the fundamental mechanical principles of magnetic stirring systems. The analysis of magnetic circuits and magnetic forces provides design references for engineering applications, identifies critical parameters for stable operation, and proposes optimization strategies. The optimized active magnet structure (axially magnetized configuration) and rotor configuration (permanent magnet-superparamagnetic material hybrid structure) were determined. These findings offer theoretical and technical foundations for engineering design and application. Closed-loop validation through theoretical, simulation, and experimental approaches confirmed that the optimized master-slave rotor configuration significantly enhances stability and magnetic field utilization efficiency. Particularly suitable for nuclear applications with stringent sealing requirements, limited space, and non-interchangeable components, this study provides valuable references for engineering implementation of magnetic stirrers in nuclear industries.

Declaration of Interest Statement

Availability of data and materials

Data available on request from the authors.

Competing interests

We declare that we have no financial and personal relationships with other people or organizations that can inappropriately influence our work, there is no professional or other personal interest of any nature or kind in any product, service and/or company that could be construed as influencing the position presented in, or the review of, the manuscript entitled.

Funding

This work was supported by China Nuclear Power Engineering Co., Ltd., Beijing Chemical Industry Research and Design Institute, Chemical Equipment Institute, Beijing 100840, China.

Authors' contributions

The authors confirm that the article has not been accepted for publishing in another journal. The authors confirms that the research in their work is original and finishes without AI, and that all the data given in the article are real and authentic. If necessary, the article can be recalled, and errors corrected.

Acknowledgements

I would like to thank Professor Dehui Wu for inspiring my interest in the development of innovative technologies. I would like to thank Ziyang Li for providing meaningful suggestions and help to me.

References

[1] E. Rajasekaran and B. Kumar, Int. J. Innov. Res. Sci. Eng. Technol. **3**, 1262 (2014).
[2] F. Yiwen and Z. Denglei, Henan Science and Technology **8**, 48 (2019).
[3] D. Xinsheng, Z. Kezhong, and X. Chenghai, Chemical Machinery **31**, 357 (2004).
[4] Z. Kezhong, Theoretical Design and Application of Magnetic Coupling Transmission Technology and Device, Chemical Industry Press, Beijing (2018) pp. 67-70.
[5] N. Xuhua, Xu Yaotian, and Fu Bin, J. Appl. Technol. **23**, 167 (2023).
[6] S. Schneider and S. Seide, Processes **11**, 3231 (2023).
[7] D. Nurhidayati, Berkala Penelitian Teknologi Kulit, Sepatu, dan Produk Kulit **23**, 7 (2024).
[8] M. S. Demirsoy, M. S. Sarıkaya, and S. Kurnaz, J. Braz. Soc. Mech. Sci. Eng. **47**, 580 (2025).
[9] Y. Öner, Sensors and Actuators A: Physical **137**, 200 (2007).
[10] O. Kalender, Y. Ege. IEEE Trans. Magn. **43**, 3579 (2007).
[11] J. Liu, D. Li, C. Zhang, L. Li, and J. Cai, Tribology International **197**, 109774 (2024).
[12] D. Li, Magnetic Fluid Seal Theory and Application, Science Press, Beijing (2010) pp. 188-190.
[13] D. J. Griffiths. Introduction to electrodynamics. Cambridge University Press, Cambridge (2023) pp. 204-205.
[14] Y. Zhen, Electrodynamics, Science Press, 2nd ed. Beijing (2003) pp. 145-146.
[15] X. Yuan, College Physics **10**, 39 (2006).